Research Article

Chemical Review and Letters
journal homepage: www.chemrevlett.com
ISSN (online): 2645-4947 (print) 2676-7279

Transition state structures of elementary reactions of benzimidazole synthesis in the presence of graphene quantum dot: A DFT study

Reza Behjatmanesh-Ardakani[1, *], Huseyn A. Imanov[2]

[1]*Department of Chemical Engineering, Faculty of Engineering, Ardakan University, P.O. Box: 184, Ardakan, Iran.*
[2]*Faculty of Natural Sciences and Agriculture, Department of Chemistry, Nakhchivan State University, Azerbaijan.*

ARTICLE INFO

Article history:
Received 29 October 2025
Received in revised form 29 November 2025
Accepted 07 December 2025

Keywords:
Benzimidazole synthesis
Reaction mechanism
LST/QST,
Transition state
Graphene catalyst

ABSTRACT

Benzimidazole is the central core for drug synthesis. Obtaining detailed information about its synthesis mechanism can help us to design new catalysts to increase synthesis yield. Our previous results showed that in the absence of any catalysts, the steps 1 and 3 in which nitrogen in phenylene diamine attack on the formic acid carbon have higher barrier energies; while, dehydration steps (steps 2 and 4) have less barrier energies. In this paper, graphene quantum dot is used as a catalyst for benzimidazole synthesis, and all elementary steps are in detail studied. Stabilization energy due to the interaction between two reactants (formic acid and phenylene diamine) in the absence and presence of graphene catalyst are -9.08 and -26.29 kcal·mol^{-1}, respectively. This causes that the rate determining step (RDS) is reduced more when graphene is used as the catalyst. The RDS for benzimidazole synthesis in the absence and presence of catalyst are 36.05 and 27.88 kcal·mol^{-1}, respectively. In addition to the RDS, all other transition structures in the presence of graphene have energies less than the total energies of isolated formic acid and phenylene diamine. Considering thermal, entropic, and solvation free energy corrections reduces the relative barrier energy by 2.18 kcal·mol^{-1}. These corrections include zero-point vibrational energy (ZPVE), thermal contributions (TS and H), and solvation free energy (ΔGsolv), which together provide a more accurate representation of the reaction energetics.

1. Introduction

Benzimidazole motifs serve as fundamental structural elements in pharmaceutical chemistry and constitute the basis of many therapeutic agents with a broad spectrum of biological actions, ranging from anticancer [1], antidepressant [2], anti-Alzheimer [3], antiallergic [4], antioxidant [5], and antiviral properties [6] to antihypertensive, anti-inflammatory [7] and antidiabetic [8] activities. Modifications to these molecules through the addition of different substituents or functional moieties enable precise control over their pharmacological behavior [9]. Investigations into structure-activity relationships (SAR) have elucidated how drug performance relates to particular patterns of substitution on the benzimidazole nucleus, thereby facilitating rational design of targeted pharmaceuticals [10].

Considerable effort has been devoted to designing novel benzimidazole derivatives to explore their therapeutic potential. For example, Jeyakkumar et al., reported berberine–benzimidazole conjugates exhibiting strong antimicrobial and antifungal effects [11]. Alasmary and co-workers prepared 1,2,5-trisubstituted benzimidazoles and evaluated their antibacterial activity. [12]. Similarly, Liu and colleagues synthesized aminopyrimidinyl benzimidazoles with notable antimicrobial activity [13], while Abdullah and collaborators analyzed how electron-donating and electron-withdrawing substituents on carboxamide and biphenyl benzimidazole analogs influence anticancer properties [14]. Numerous investigations have explored benzimidazole derivatives across anticancer, antimicrobial, and related pharmacological areas [15-22].

Several clinically important drugs such as Oxibendazole, Thiabendazole, xParbendazole, Omeprazole, and Mebendazole rely on the benzimidazole pharmacophore to deliver anthelmintic, antifungal,

* Corresponding author E-mail: behjatmanesh@ardakan.ac.ir
https://doi.org/10.22034/crl.2025.556122.1720

polymerase-inhibition, antiparasitic, and antiulcer effects, respectively. This underscores the central role of benzimidazole synthesis in pharmaceutical innovation. Detailed characterization of the electronic properties of benzimidazole and its associated transition states during synthesis could enable the development of new synthetic methodologies, reducing cost and improving efficiency.

Elucidating a benzimidazole synthesis mechanism begins with identifying elementary steps and transition states. Although the overall synthesis pathway is established, microscopic details—such as the relative energies of transition states and intermediates—remain incompletely characterized. For instance, Mohanty and colleagues investigated azo-benzimidazole formation [23], while Jin and co-workers described copper-catalyzed intramolecular N-arylation approaches [24]. Keri and co-workers highlighted environmentally friendly methods for functionalized benzimidazoles, outlining plausible mechanisms and directions for future work [25].

Conventionally, benzimidazoles form by condensing o-phenylenediamine with aldehydes or carboxylic acids. This process involves nucleophilic attack by the diamine nitrogens on carbonyl carbons, followed by dehydration to establish C–N bonds. The cyclization stage typically comprises four key elementary steps, each with a distinct transition state. Dehydration steps often require less energy than C–N bond-forming steps; however, comprehensive microscopic insights into the overall mechanism remain limited. Addressing these gaps calls for quantum-mechanical analyses to achieve atomistic understanding. Density functional theory (DFT) serves as a powerful tool for constructing models to investigate these gaps. Prior research demonstrates that DFT methods are effective in designing both periodic [26-29] and non-periodic catalysts [30-34]. Furthermore, DFT facilitates understanding the photocatalytic properties of doped inorganic oxides [35-40], enables the optimization of materials for batteries [41, 42], and assist in the rational design of novel drugs [43], advanced drug carriers [44-51], removing air pollutants [52] and innovative sensors [53-57].

In the present work, all elementary reactions involved in benzimidazole synthesis are investigated using first-principles DFT. Detailed electronic properties of reactants, intermediates, transition states, and products are reported. The graphene quantum dot was employed as a novel catalyst to examine the changes in the energy barrier during benzimidazole synthesis. While graphene has been utilized in numerous experimental studies, to date, no reports have addressed its impact on the mechanistic pathway of benzimidazole formation. The paper is organized as follows: Section 2 outlines the computational approach and software employed; Section 3 provides an overview of the proposed mechanism together with identified transition states and their relative energy profiles; the concluding section summarizes the principal findings.

2. Materials and Methods

To explore the benzimidazole synthesis mechanism and examine the electronic characteristics of the participating species, three complementary computational programs were applied. The structures of molecules and all transition states were optimized using DMol³ program [58], allowing the determination of reaction energy barriers and profiles. Gaussian program [59] was employed to compute wavefunctions for the optimized geometries, and these results were subsequently analyzed through MultiWFN program [60] to perform charge density and topological evaluations following the quantum theory of atoms in molecules (QTAIM). The graphical construction and visualization of Gaussian input and output files were carried out using GaussView program [61].

In DMol³ calculations, the geometries of all species – reactants, intermediates, and products – were optimized within the framework of the Perdew–Burke–Ernzerhof (PBE) exchange-correlation functional [62]. To appropriately describe van der Waals interactions, Grimme's DFT-D2 empirical dispersion correction was included [63]. Since transition state identification is computationally demanding, the PBE functional was chosen because it offers a well-established balance between computational efficiency and accuracy for modeling catalytic reactions [39, 64-67]. The valence orbitals were represented by the double numeric plus polarization (DNP) basis set, while core electrons were treated using density functional semicore pseudopotentials (DSPP). The default orbital cutoff parameter was retained. The energy convergence criteria for the electronic cloud and geometry optimizations were set to 10^{-6} ans 10^{-5} Ha, respectively. The force convergence threshold was set to 0.002 Ha/Å. The self-consistent field (SCF) charge and spin mixing parameters were 0.5 and 0.2, respectively. The displacement convergence for geometry optimization was fixed at 0.005 Å. Transition states were initially located using the Linear Synchronous Transit (LST) method and subsequently refined by the Quadratic Synchronous Transit (QST) procedure. The root mean square (RMS) convergence for LST/QST was set to 0.003 Ha/Å. Fifteen images were employed for transition state confirmation. The parameters S6 and d for Grimm's D2 dispersion correction were set to 0.75 and 20, respectively, while thermal occupation was assigned a value of 0.008.

For Gaussian-based quantum chemical computations, wavefunctions used in QTAIM analyses were generated with the B3LYP hybrid density functional [68-70] together with the triple-zeta valence plus polarization Def2-TZVP basis set [71]. This level of theory is recognized as reliable for charge calculations [72-74].

Standard numerical integration settings (99,590 grid points) and SCF convergence criteria were employed in all Gaussian calculations. All other parameters for the Gaussian program calculations were maintained at their default settings. The Gibbs free anergy and its difference values for reaction and activation energies were computed using the following equations:

$$G = E_{elec.} + ZPVE + H - TS + \Delta G_{solv.} \quad (1)$$

$$\Delta G = \Delta E_{elec.} + \Delta ZPVE + \Delta H - T\Delta S + \Delta\Delta G_{solv.} \quad (2)$$

Vibrational frequencies were calculated via the finite difference method with a displacement parameter of 0.0053 Å. Literature reports demonstrate that including solvent effects in DFT calculations yields results that are closer to experimental values [75, 76]. Accordingly, solvation free energies were incorporated using the Conductor-like Polarizable Continuum Model (CPCM) to account for solvent effects in the calculations.

3. Results and Discussion

3.1. Mechanistic overview

Figure 1 illustrates the widely recognized reaction pathway for synthesizing benzimidazole, which originates from the condensation of phenylenediamine and formic acid through four elementary reaction steps. Figure 2 represents these four elementary steps, catalyzed by the graphene quantum dot. S0 corresponds to the initial mixture graphene, phenylenediamine, and formic acid.

The state labeled R1 is obtained after both formic acid and phenylenediamine are physically adsorbed onto the graphene surface. In the first step (S1) a nucleophilic attack is occurred in which one of the phenylenediamine nitrogen atoms donates its lone pair to the carbonyl carbon of formic acid, producing a tetrahedral intermediate. Concurrently, a hydrogen atom from the amino group is transferred to the carbonyl oxygen, yielding a hydroxyl group.

Subsequently, a water molecule is generated through the combination of an adjacent hydrogen atom with the hydroxyl group (S2), producing a new carbonyl moiety and facilitating structural rearrangement toward cyclization.

In the third step (S3), the remaining nitrogen center of phenylenediamine performs a second nucleophilic attack on this newly formed carbonyl carbon, creating another C–N linkage that drives the molecular framework toward an imidazole ring. The final step (S4) involves the elimination of an additional water molecule, culminating in the formation of the benzimidazole skeleton. The dashed lines shown in Figure 1 and 2 merely illustrate conceptual interactions between the graphene catalyst and the evolving intermediates.

The explicit nature of catalyst–substrate interactions is analyzed in detail in the subsequent discussion by QTAIM.

3.2. Transition states and electronic property analyses

Figures 3–6 display and topological graphs of the optimized geometries corresponding to the initial, transition, and final configurations involved in the four elementary reactions schematically outlined in Figure 2. In the R1 complex, nine noncovalent interactions are identified: three π–π interactions between graphene and phenylenediamine (C6···C38, C4···C46, C2···C57), two hydrogen bonds (O18···H11, O18···H10), three lone pair–π (LP–π) interactions involving N7, N8, and O18 lone pairs, and one hydrogen–π (H–π) interaction (H20···C51). These interactions collectively link formic acid, phenylenediamine, and graphene within the complex.

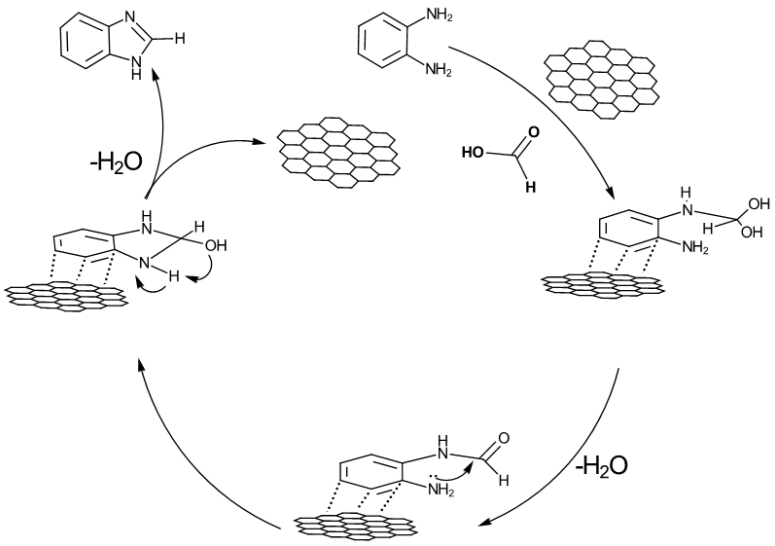

Fig. 1. Proposed reaction pathway for benzimidazole synthesis. The diagram illustrates four distinct transition states (TS1–TS4), with the formation of two water molecules as byproducts during the process.

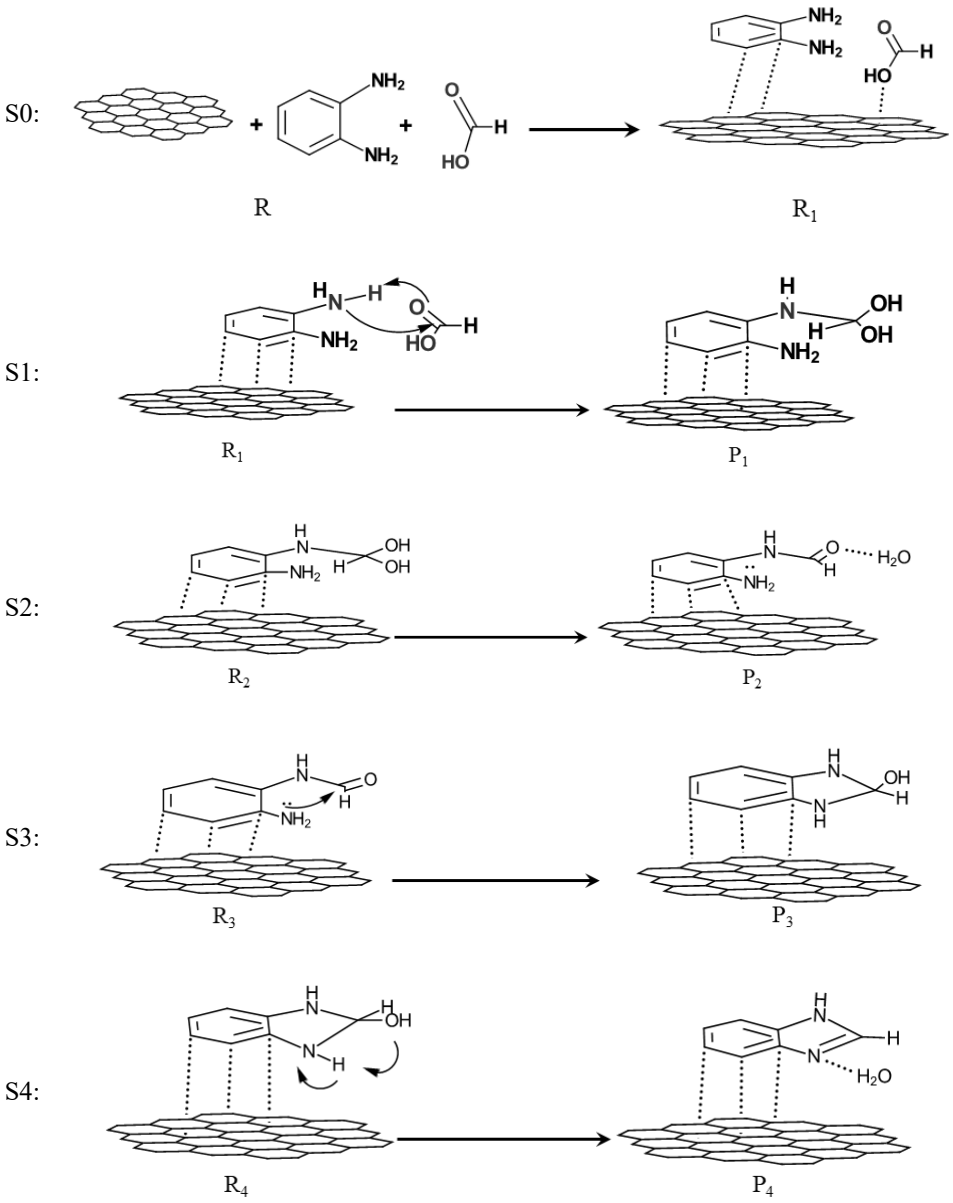

Fig. 2. Proposed mechanism illustrating the four elementary steps involved in benzimidazole synthesis catalyzed by graphene nanocatalyst.

The overall energy associated with these nine noncovalent interactions is found to be −26.29 kcal·mol⁻¹, indicating that the collective adsorption of formic acid and phenylenediamine is exothermic. The total energy of the isolated species (formic acid, phenylenediamine, and graphene quantum dot) was taken as the reference energy. All reported energies in the reaction coordinate profile are expressed relative to this reference energy. In Figures 3–6, the topological graphs of the noncovalent interactions, calculated by QTAIM, are presented in both side and top views to provide a clear visualization of these interactions.

The absolute and relative reaction and activation energies, together with the transition state coordinates for all four elementary reactions illustrated schematically in Figure 2, are summarized in Table 1. As stated previously, the reference energy used to calculate relative energies is the total energy of three isolated components: formic acid, phenylenediamine, and graphene quantum dot (denoted as R in the S0 step of Figure 2). All values in parentheses correspond to the benzimidazole synthesis in the absence of any catalyst, as reported in our previous publication [77]. A brief examination of this table, comparing the data obtained in the presence and absence of the catalyst, reveals that graphene can significantly reduce the transition state activation energy for each elementary step of the benzimidazole synthesis. Each reaction step is discussed in detail below, focusing on the geometric and electronic properties of the reactants, transition states, and products involved in each step.

Figure 3 focuses on the first elementary reaction, where nitrogen atom N8 attacks the carbon atom C17 of formic acid. Concurrently with this approach, hydrogen

atom H11 migrates toward the oxygen O18 of formic acid. In contrast to the first elementary reaction without the catalyst, where the rotation of formic acid leads to the disruption of two hydrogen bonds (O···H and H···C), the presence of graphene prevents the rotation of formic acid and preserves the intermolecular hydrogen bond. The relative barrier and reaction energies listed in Table 1 indicate that, in the presence of graphene, the first elementary step is both kinetically and thermodynamically favorable.

Although the reaction is endothermic, its relative energy with respect to the reference state (R in the S0 step, representing the isolated components) is −14.34 kcal·mol^{-1}, making the reaction thermodynamically favorable. The QTAIM analysis shown in Figure 3 reveals that the H11 atom simultaneously interacts with N7, O18, and C93. The electron densities at the bond critical points (BCPs) for N7···H11, O18···H11, C59···H12, and C93···H11 are ρ = 0.178, 0.122, 0.012, and 0.010 a.u., respectively. In addition to TS1, H···C interactions are also observed in the R1 and P1 topological graphs. In R1, the C51···H20 bond exhibits an electron density of 0.013 a.u. at the BCP, while in P1, the C61···H20 and C93···H11 interactions show electron densities of 0.010 and 0.012 a.u., respectively.

Significant π–π interactions are also observed between the graphene catalyst and the reactant molecules. In the R1 configuration, six notable π–π contacts are identified between the following atom pairs: C2···C57, C4···C46, C6···C38, N8···C59, N7···C91, and O18···C90. The corresponding electron densities at the BCPs for these interactions are 0.0071, 0.0068, 0.0071, 0.0089, 0.0074, and 0.0048 a.u., respectively. In the TS1 structure, π–π interactions are identified between the following atomic pairs: C2···C57, C3···C47, C4···C46, C6···C38, and N7···C29. The electron densities at the bond critical points (BCPs) for these interactions are 0.0071, 0.0071, 0.0058, 0.0057, and 0.0053 atomic units (a.u.), respectively.

Table 1. Activation barrier energies (absolute and relative), reaction energies (absolute and relative), and the locations of transition states for the four elementary steps in benzimidazole synthesis in the presence of graphene quantum dot. Energies and frequencies are presented in kcal·mol^{-1} and cm^{-1}, respectively. Values in parentheses correspond to the reactions conducted without the catalyst.[1]

Reaction	Absolute Barrier Energy	Relative Barrier Energy	Absolute Reaction Energy	Relative Reaction Energy	TS location	Imag. Freq.
S0	0.00 (0.00)	0	-26.29 (-9.08)	-26.29 (-9.08)	-	-
S1	+1.74 (+41.93)	-24.55 (+32.85)	+11.95 (+11.84)	-14.34 (-6.32)	0.29 (0.67)	-48
S2	+6.56 (+27.97)	-7.98 (+21.65)	-11.99 (-9.08)	-26.32 (-15.40)	0.41 (0.49)	-269
S3	+46.11 (+45.85)	+25.78 (+36.00)	+13.85 (+11.02)	-6.50 (+1.17)	0.65 (0.52)	-1024
S4	-6.34 (+33.45)	-11.48 (+34.62)	-13.71(-10.55)	-18.84 (-9.38)	0.31 (0.2)	-35

[1]All absolute and relative barrier and reaction energies correspond to electronic energies ($E_{elec.}$)

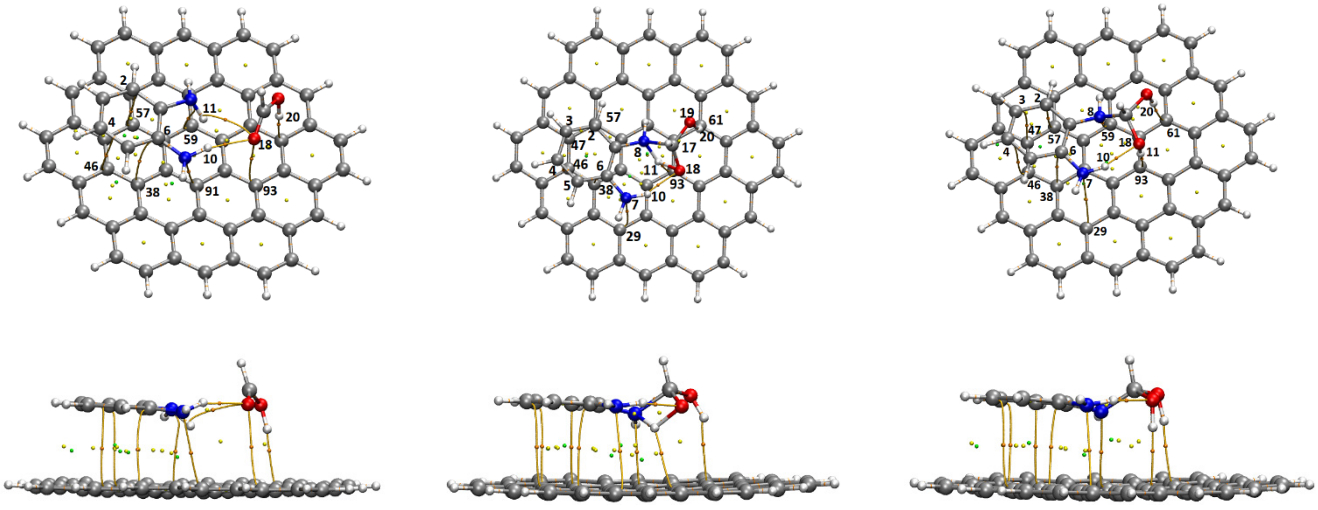

Fig. 3. Topological analyses from top and side views for the initial reactant (R1, left), transition state (TS1, middle), and product (P1, right) of the first elementary reaction (S1).

In the P1 structure, the π–π interactions are observed between the atomic pairs C2···C57, C3···C47, C4···C46, C6···C38, N7···C29, and N8···C59, with corresponding electron densities at the bond critical points (BCPs) of 0.0077, 0.0074, 0.0057, 0.0061, 0.0060, and 0.0110 atomic units (a.u.), respectively. These interactions bring formic acid and phenylenediamine into close proximity, restricting the rotation of the reactants and thereby facilitating C–N bond formation in the S1 step.

Table 1 indicates that the TS1 location value of 0.29 suggests TS1 is structurally more similar to the R1 reactant. In contrast, for the system without a catalyst, the TS1 location is 0.67 [77], implying that the transition state structure more closely resembles the product. The QTAIM charges of N8 and C17 are -1.06 and +1.56 in R1, -1.03 and +1.27 in TS1, and -1.04 and +1.27 |e|, respectively.

The S2 elementary step, analogous to S1, is both thermodynamically and kinetically favorable. The relative energy of TS2 is approximately 30 kcal·mol^{-1} lower than the corresponding transition state energy in the absence of catalyst. The relative reaction energy for S2 is approximately 11 kcal·mol^{-1} lower than that of the corresponding step without the catalyst. Figure 4 shows the topological graphs of R2, TS2, and P2 for S2 elementary reaction. This figure illustrates various hydrogen bonds and π–π interactions between graphene and the intermediate species. In the R2 structure, two hydrogen bonds are present: H10···O19 and H11···C90, with electron densities at BCPs of 0.014 and 0.0091 a.u., respectively. The π–π interactions in R2 involve the following pairs: C1···C39, C5···C29, C3···C37, and N7···C30, with corresponding BCP electron densities of 0.0067, 0.0064, 0.0067, and 0.0062 a.u., respectively. The hydrogen bonds in TS2 are H10···O19 and H11···C93 with the electron densities of 0.020 and 0.013 a.u., respectively. There are six π–π interactions containing C1···C39, C2···C48, C3···C37, C4···C26, C5···C28, and N7···C30 with the electron densities of 0.0065, 0.0059, 0.0081, 0.0041, 0.0059, and 0.0052, respectively. For P2 there are eight noncovalent interactions, three hydrogen bonds and 5 π–π interactions. The hydrogen bonds are H10···O19, H20···O19, and H11···C93 with the electron densities of 0.032, 0.013, and 0.013 a.u., respectively. The π–π interactions are C2···C48, C1···C39, C3···C37, C5···C28, and N7···C30 with the electron densities of 0.0071, 0.0062, 0.0085, 0.0058, and 0.0055 a.u., respectively. H20···O19 related to the hydrogen bond between leaving water molecule and the other oxygen. The energy associated with this hydrogen bond corresponds to the energy difference between the P2 and R3 configurations, amounting to 6 kcal·mol^{-1}.

Figure 5 presents the topological graph for the S3 elementary reaction. This step is the most significant in the benzimidazole synthesis, as it possesses the highest activation energy along the reaction coordinate. Consistent with the reaction conducted without a catalyst, S3 remains the rate-determining step (RDS) in the presence of graphene, dictating the overall reaction rate. The relative activation energy of TS3 in the presence of graphene is approximately 10 kcal·mol^{-1} lower than that of the equivalent transition state without the catalyst. Additionally, its relative reaction energy is about 8 kcal·mol^{-1} more exothermic compared to the value observed in the absence of graphene. In R3 there are five π–π interactions and two hydrogen bonds. The hydrogen bonds are H10···O17 and H18···C59 with the electron densities of 0.036 and 0.0036 a.u., respectively. The π–π interactions are: C1···C46, C2···C54, C4···C44, C4···C43, and N7···C88 with the electron densities of 0.0065, 0.0067, 0.0071, 0.0069, and 0.0082 a.u., respectively. In TS3 there are two hydrogen bonds and five π–π interactions.

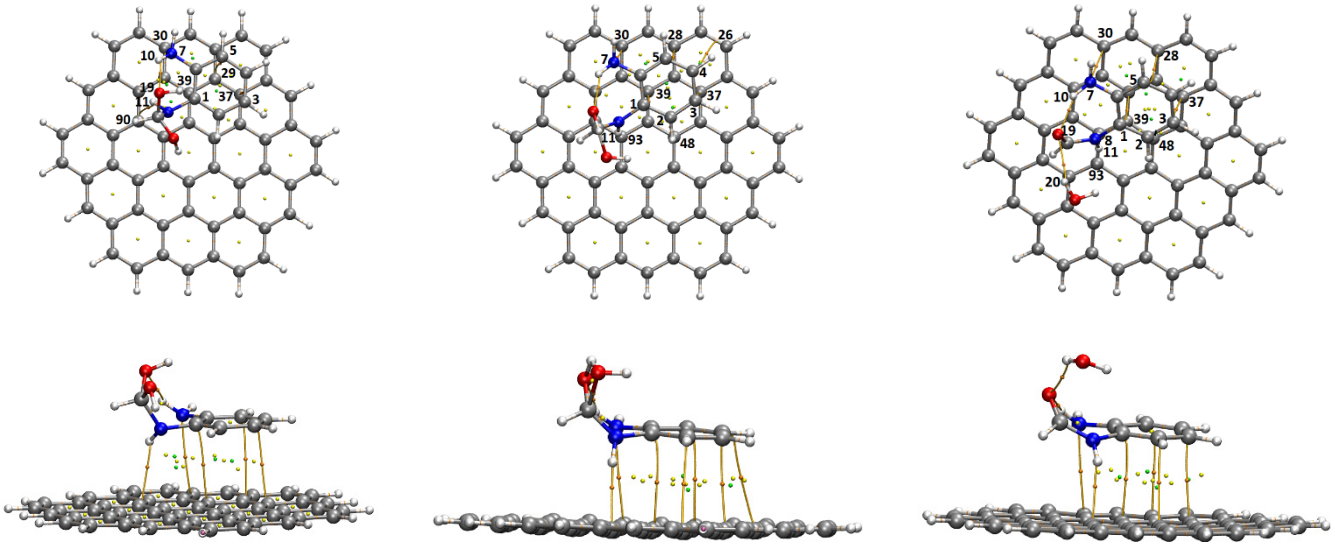

Fig. 4. Topological analyses from top and side views for the initial reactant (R2, left), transition state (TS2, middle), and product (P2, right) of the second elementary reaction (S2).

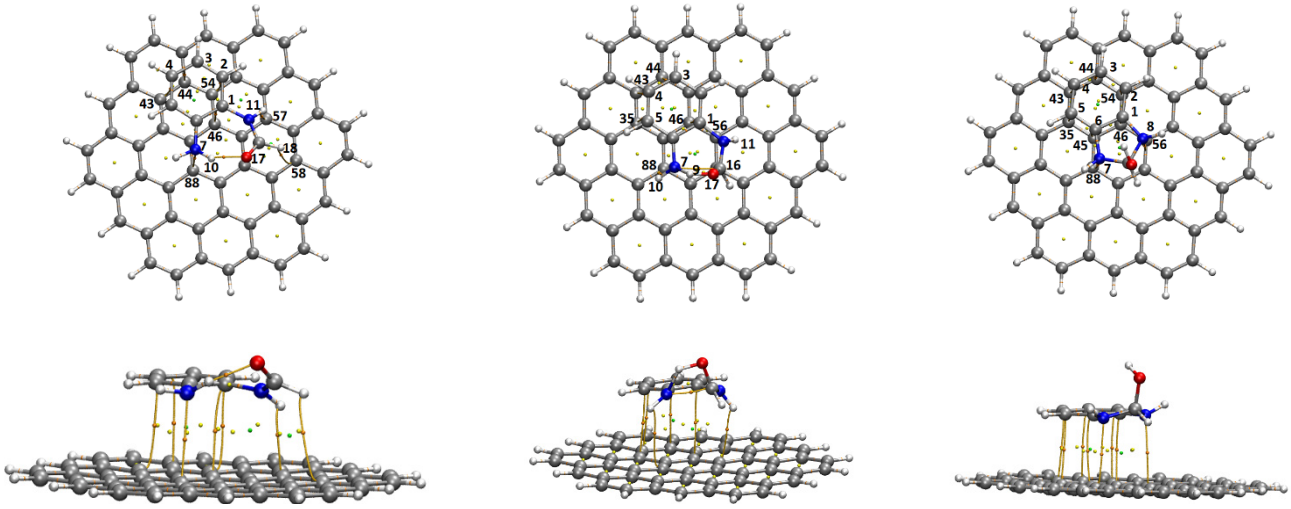

Fig. 5. Topological analyses from top and side views for the initial reactant (R3, left), transition state (TS3, middle), and product (P3, right) of the third elementary reaction (S3).

The hydrogen bonds are H10···C88 and H11···C56 with the electron densities of 0.0048 and 0.0071 a.u., respectively. The π–π interactions are: C1···C46, C3···C44, C4···C43, C5···C35, and N7···C16 with the electron densities of 0.0049, 0.0069, 0.0075, 0.0072, and 0.0064 a.u., respectively. P3 has eight π–π interactions without any hydrogen bond. The π–π interactions are C1···C46, C2···C54, C3···C44, C4···C43, C5···C35, C6···C45, N7···C88, and N8···C56 with the electron densities of 0.0064, 0.0060, 0.0071, 0.0078, 0.0081, 0.0071, 0.0082, and 0.0068 a.u., respectively.

The final elementary step, S4, exhibits a relative activation barrier approximately 23 kcal·mol^{-1} lower than that of the analogous step without the catalyst. The relative reaction energy indicates that, in the presence of graphene, S4 is twice as exothermic as the corresponding reaction conducted in the absence of graphene. Figure 6 shows the topological graphs for R4, TS4, and P4. There are four π–π interactions and a hydrogen bond in R4, five π–π interactions and one hydrogen bond in TS4, and five π–π interactions and three hydrogen bonds in P4. The hydrogen bond in R4 is H18···C47 with the electron density of 0.0087 atomic unit. The π–π interactions in R4 are C2···C46, C4···C35, C6···C88, N7···C87, and N8···C89 with the electron densities of 0.0076, 0.0076, 0.0078, 0.0075, 0.0084, and 0.0076 a.u., respectively. The hydrogen bond in TS1 is H9···N7 with 0.0088 a.u., and the π–π interactions are C2···C46, C4···C35, C6···C88, C16···C87, and N8···C89 with the electron densities of 0.0069, 0.0076, 0.0080, 0.0097, 0.0083, and 0.0088 a.u., respectively.

In P4 five interactions belong to the benzimidazole and three interactions belong to leaving water molecule. The π–π interactions in P4 are C2···C46, C4···C35, C6···C88, C16···C87, and N8···C89 with the electron densities of 0.0082, 0.0066, 0.0066, 0.0074, and 0.0086 a.u., respectively, and the hydrogen bonds are H9···C27, H10···N7, H12···O17 with the electron densities of 0.010, 0.032, and 0.0070 a.u., respectively.

The calculated energy diagram for the benzimidazole formation pathway catalyzed by graphene is depicted in Figure 7. As discussed earlier, the label "R" corresponds to the initial configuration, which includes separate graphene, formic acid, and phenylenediamine and serves as the zero-point energy reference. "P4" denotes the final state of the consecutive four-step process in which benzimidazole and a water molecule are attached to the graphene sheet.

Regeneration of the catalyst is achieved when P4 transitions to P, producing free graphene, benzimidazole, and water. The energy profile reveals an overall activation energy of 25.78 kcal·mol^{-1} for the conversion of phenylenediamine and formic acid into benzimidazole, with an associated reaction energy of -18.84 kcal·mol^{-1}.

The energy needed to dissociate the benzimidazole-water-graphene complex amounts to 33.32 kcal·mol^{-1}. Since the overall relative reaction energy, -18.84 kcal·mol^{-1}, is released during the P4 synthesis step, only about 14.48 kcal·mol^{-1} is needed for regenerating catalyst.

3.3. Frequency analysis and solvation effects

To evaluate the thermal (enthalpy and zero-point vibrational energy, *ZPVE*), entropic (*TS*), and solvation free energy (ΔG_{solv}) contributions to the relative energies of reactants, products, and transition states, all these terms were calculated for each species. Table 2 summarizes the corrections applied to the reaction and transition state energies. Considering the correction terms alters the relative barrier and reaction energies for all steps. Only for TS1 does the barrier energy increases, and this increase is minimal at +0.68 kcal·mol^{-1}. For the other three steps, the transition state barrier energies decrease, with the largest reductions observed for TS2 and TS4, where a water molecule is released as a by-product.

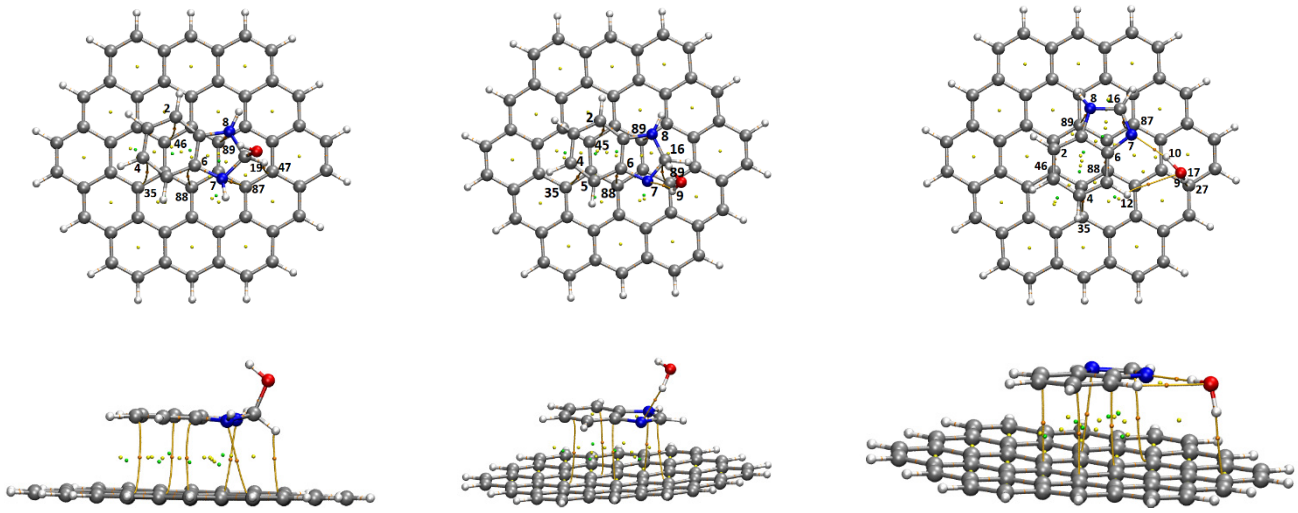

Fig. 6. Topological analyses from top and side views for the initial (R_4, left)), transition state (TS_4, middle), and product (P_4, right) of the fourth elementary reaction (S4).

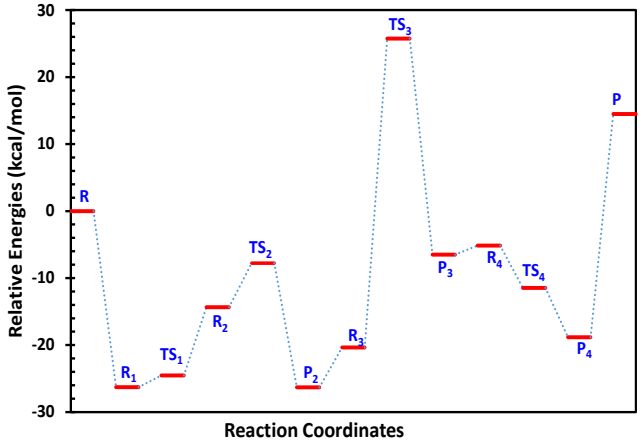

Fig. 7. Energy profile diagram depicting the multistep reaction mechanism for benzimidazole synthesis from phenylenediamine and formic acid catalyzed by the graphene quantum dot.

Table 2. The correction terms ($\Delta H+\Delta ZPVE-T\Delta S+\Delta\Delta G_{solv}$) for reactions S1 to S4, transition states TS1 to TS4, and their relative barrier free energies, all expressed in kcal·mol^{-1}.

Reaction	Correction	Relative Reaction Free Energy	Transition State	Correction	Relative Barrier Free energy
S1	+2.05	-12.28	TS1	+0.68	-23.86
S2	-3.44	-29.76	TS2	-3.20	-10.98
S3	-0.63	-7.14	TS3	-2.18	+23.58
S4	+1.64	-17.20	TS4	-8.17	-17.20

Including solvation free energy stabilizes these transition states by accounting for charge interactions between the solvation model and the water hydrogens and oxygen in TS2 and TS4.

The rate-determining step (RDS), TS3, is also lowered when entropic and solvation free energy contributions are considered. With a barrier energy of +23.58 kcal·mol^{-1} for the RDS in benzimidazole synthesis, it is possible to estimate the minimum temperature required for a 100% yield. Applying the Redhead equation [78] and assuming a pre-exponential factor of 10^{13} s^{-1}, the temperature for 100% yield is calculated to be 332 K (59 °C). For a 90% yield (α=0.9) in a first-order reaction, the following relations apply:

$$ln\left(\frac{[A]}{[A_0]}\right) = -kt,\ k = Ae^{\frac{-E_a}{RT}}, [A] = [A_0](1-\alpha) \quad (3)$$

and

$$ln(1-\alpha) = -kt = -\left(Ae^{\frac{-E_a}{RT}}\right)t \quad (4)$$

Considering a reaction time t=3600 s, a pre-exponential factor A=10^{+13} s^{-1}, an activation energy

E_a=23.58 kcal·mol^{-1}, and the gas constant R=1.987 cal·mol^{-1}·K^{-1}, the calculated temperature is approximately 316 K (43°C). It is important to note that the uncertainty associated with the Redhead equation is at least ±5%.

4. Conclusion

This work presents a comprehensive quantum chemical analysis of the multistep benzimidazole formation mechanism, proceeding from phenylenediamine and formic acid in the presence of a graphene quantum dot catalyst. The proposed pathway involves four consecutive elementary reactions: initial C–N bond creation, two successive dehydration events, and ultimate cyclization to form the heterocycle. Graphene acts as a catalyst by exothermically adsorbing both formic acid and phenylenediamine, resulting in a release of 26.29 kcal·mol^{-1}. Computational results demonstrate that graphene effectively stabilizes the first transition state (TS1), reducing its activation energy from 41.93 to 1.74 kcal·mol^{-1} (with the relative energy shift from 32.85 to -34.55 kcal·mol^{-1}). The rate-determining step is identified as the third elementary process (S3), where ring formation occurs.

Initial exothermic adsorption contributes to lowering the total synthesis barrier from 46.11 to 25.78 kcal·mol^{-1} when a graphene catalyst is present, corresponding to an activation temperature requirement near 158 °C. Additionally, theoretical predictions indicate that conducting the reaction at 50 °C yields up to 90%, which is considerably higher than observed without the catalyst. Quantum Theory of Atoms in Molecules (QTAIM) analysis further reveals numerous van der Waals contacts (electron density at bond critical points below 0.01 a.u.) stemming from π–π or lone pair–π interactions between graphene and formic acid, phenylenediamine, and intermediate compounds. These weak interactions seem to orient reaction intermediates more favorably, thereby facilitating reduced energy barriers throughout the transformation.

In the present study, no defects or functional groups such as OH and COOH were considered. These functional groups could potentially interact with various groups in formic acid, phenylenediamine, and all reaction intermediates. Consequently, the presence of OH, COOH, or defects may alter both barrier and reaction energies. Readers are encouraged to explore the effects of these functional groups on the benzimidazole synthesis mechanism. In our future work, we aim to investigate the influence of these functional groups on reactants, products, intermediates, and all transition states.

Acknowledgments

The authors gratefully acknowledge the support provided by Ardakan university.

References

[1] H. Atmaca, S. İlhan, M. B. Batır, Ç. Ç. Pulat, A. Güner and H. Bektaş, Novel benzimidazole derivatives: Synthesis, in vitro cytotoxicity, apoptosis and cell cycle studies. *Chem. Biol. Interact.*, 327 (2020) 109163. https://doi.org/10.1016/j.cbi.2020.109163

[2] M. A. Tantray, I. Khan, H. Hamid, M. S. Alam, A. Dhulap and A. Kalam, Synthesis of benzimidazole-linked-1,3,4-oxadiazole carboxamides as GSK-3β inhibitors with in vivo antidepressant activity. *Bioorg. Chem.*, 77 (2018) 393-401. https://doi.org/10.1016/j.bioorg.2018.01.040

[3] Y. Fang, H. Zhou, Q. Gu and J. Xu, Synthesis and evaluation of tetrahydroisoquinoline-benzimidazole hybrids as multifunctional agents for the treatment of Alzheimer's disease. *Eur. J. Med. Chem.*, 167 (2019) 133-145. https://doi.org/10.1016/j.ejmech.2019.02.008

[4] M. L. Richards, S. C. Lio, A. Sinha, K. K. Tieu and J. C. Sircar, Novel 2-(Substituted phenyl)benzimidazole Derivatives with Potent Activity against IgE, Cytokines, and CD23 for the Treatment of Allergy and Asthma. *J. Med. Chem.*, 47 (2004) 6451-6454. https://doi.org/10.1021/jm049288j

[5] N. Karmaker, D. N. Lira, B. K. Das, U. Kumar and A. S. S. Rouf, Synthesis and Antioxidant Activity of Some Novel Benzimidazole Derivatives. *Dhaka Univ. J. Pharm. Sci.*, 16 (2018) 245-249. https://doi.org/10.3329/dujps.v16i2.35263

[6] A. Singh, D. Yadav, M. Yadav, A. Dhamanage, S. Kulkarni and R. K. Singh, Molecular Modeling, Synthesis and Biological Evaluation of N-Heteroaryl Compounds as Reverse Transcriptase Inhibitors Against HIV-1. *Chem. Biol. Drug Des.*, 85 (2015) 336-347. https://doi.org/10.1111/cbdd.12397

[7] N. A. Al-Masoudi, N. N. A. Jafar, L. J. Abbas, S. J. Baqir and C. Pannecouque, Synthesis and anti-HIV Activity of New Benzimidazole, Benzothiazole and Carbohyrazide Derivatives of the anti-Inflammatory Drug Indomethacin. *Z. Naturforsch., B*, 66 (2011) 953-960. https://doi.org/10.1515/znb-2011-0914

[8] H. Sadaf, D. Imtiaz ud, M. Fettouhi, A. Fazal, S. Ahmad, B. A. Farooqi et al., Synthesis, crystal structures and biological activities of palladium(II) complexes of benzimidazole and 2-methylbenzimidazole. *Polyhedron*, 170 (2019) 537-543. https://doi.org/10.1016/j.poly.2019.06.025

[9] B. Pathare and T. Bansode, Review- biological active benzimidazole derivatives. *Results Chem.*, 3 (2021) 100200. https://doi.org/10.1016/j.rechem.2021.100200

[10] S. R. Brishty, M. J. Hossain, M. U. Khandaker, M. R. I. Faruque, H. Osman and S. M. A. Rahman, A Comprehensive Account on Recent Progress in Pharmacological Activities of Benzimidazole Derivatives. *Front. Pharmacol.*, 12 (2021). https://doi.org/10.3389/fphar.2021.762807

[11] P. Jeyakkumar, L. Zhang, S. R. Avula and C.-H. Zhou, Design, synthesis and biological evaluation of berberine-benzimidazole hybrids as new type of potentially DNA-targeting antimicrobial agents. *Eur. J. Med. Chem.*, 122 (2016) 205-215. https://doi.org/10.1016/j.ejmech.2016.06.031

[12] F. A. S. Alasmary, A. M. Snelling, M. E. Zain, A. M. Alafeefy, A. S. Awaad and N. Karodia, Synthesis and Evaluation of Selected Benzimidazole Derivatives as Potential Antimicrobial Agents. *Molecules*, 20 (2015) 15206-15223. https://doi.org/10.3390/molecules200815206

[13] H.-B. Liu, W.-W. Gao, V. K. R. Tangadanchu, C.-H. Zhou and R.-X. Geng, Novel aminopyrimidinyl benzimidazoles as potentially antimicrobial agents: Design, synthesis and biological evaluation. *Eur. J. Med. Chem.*, 143 (2018) 66-84. https://doi.org/10.1016/j.ejmech.2017.11.027

[14] I. Abdullah, C. F. Chee, Y.-K. Lee, S. S. R. Thunuguntla, K. Satish Reddy, K. Nellore et al., Benzimidazole derivatives as potential dual inhibitors for PARP-1 and DHODH. *Bioorg. Med. Chem.*, 23 (2015) 4669-4680. https://doi.org/10.1016/j.bmc.2015.05.051

[15] G. R. Morais, E. Palma, F. Marques, L. Gano, M. C. Oliveira, A. Abrunhosa et al., Synthesis and Biological Evaluation of Novel 2-Aryl Benzimidazoles as Chemotherapeutic Agents. *J. Heterocycl. Chem.*, 54 (2017) 255-267. https://doi.org/10.1002/jhet.2575

[16] U. Acar Çevik, B. N. Sağlık, B. Korkut, Y. Özkay and S. Ilgın, Antiproliferative, Cytotoxic, and Apoptotic Effects of New Benzimidazole Derivatives Bearing Hydrazone Moiety. *J. Heterocycl. Chem.*, 55 (2018) 138-148. https://doi.org/10.1002/jhet.3016

[17] R. Kankate, A. Pagare, R. Kakad and P. Gide, Synthesis and biological evaluation of benzimidazolyl biphenyl derivatives as antihypertensive agents. *Int. J. Chem. Concepts*, 2 (2016) 111-119. https://doi.org/10.4172/2161-0444.1000243

[18] R. Sharma, A. Bali and B. B. Chaudhari, Synthesis of methanesulphonamido-benzimidazole derivatives as gastro-sparing antiinflammatory agents with antioxidant effect. *Bioorg. Med. Chem. Lett.*, 27 (2017) 3007-3013. https://doi.org/10.1016/j.bmcl.2017.05.017

[19] P. Sethi, Y. Bansal and G. Bansal, Synthesis and PASS-assisted evaluation of coumarin–benzimidazole derivatives as potential anti-inflammatory and anthelmintic agents. *Med. Chem. Res.*, 27 (2018) 61-71. https://doi.org/10.1007/s00044-017-2036-1

[20] M. Gaba and C. Mohan, Design, synthesis and biological evaluation of novel 1, 2, 5-substituted benzimidazole derivatives as gastroprotective anti-inflammatory and analgesic agents. *Med. Chem.*, 5 (2015) 058-063. http://doi.org/10.4172/2161-0444.1000243

[21] N. El-Gohary and M. Shaaban, Synthesis and biological evaluation of a new series of benzimidazole derivatives as antimicrobial, antiquorum-sensing and antitumor agents. *Eur. J. Med. Chem.*, 131 (2017) 255-262. https://doi.org/10.1016/j.ejmech.2017.03.018

[22] L. R. Singh, S. R. Avula, S. Raj, A. Srivastava, G. R. Palnati, C. K. M. Tripathi et al., Coumarin–benzimidazole hybrids as a potent antimicrobial agent: synthesis and biological elevation. *J. Antibiot.*, 70 (2017) 954-961. https://doi.org/10.1038/ja.2017.70

[23] S. K. Mohanty, A. Khuntia, N. Yellasubbaiah, C. Ayyanna, B. Naga Sudha and M. S. Harika, Design, synthesis of novel azo derivatives of benzimidazole as potent antibacterial and anti tubercular agents. *Beni-Suef Univ. J. Basic Appl. Sci.*, 7 (2018) 646-651. https://doi.org/10.1016/j.bjbas.2018.07.009

[24] X. Jin, Y. Lin and R. P. Davies, On the mechanism of benzimidazole synthesis via copper-catalysed intramolecular N-arylation. *Catal. Sci. Technol.*, 13 (2023) 7181-7189. https://doi.org/10.1039/D3CY00767G

[25] R. S. Keri, V. Adimule, P. Kendrekar and B. S. Sasidhar, The Nano-Based Catalyst for the Synthesis of Benzimidazoles. *Top. Catal.* (2022). https://doi.org/10.1007/s11244-022-01562-0

[26] R. Behjatmanesh-Ardakani, Periodic and non-periodic DFT modeling of CO reduction on the surface of Ni-doped graphene nanosheet. *Mol. Catal.*, 455 (2018) 239-249. https://doi.org/10.1016/j.mcat.2018.06.008

[27] R. Behjatmanesh-Ardakani and T. T. Magkoev, SO2 adsorption and its direct proportional dissociation on the Cu(100), Cu(110), and Cu(111) surfaces: a periodic DFT study. *Chem. Rev. Lett.*, 7 (2024) 873-883. https://doi.org/10.22034/crl.2024.467740.1380

[28] A. A. Muhammad and U. Umar, Adsorption of SO2 and NO2 on ZrO2 (110) Surface: Density Functional Theory and Molecular Dynamic Simulation Studies. *J. Chem. Lett.*, 3 (2022) 135-143. https://doi.org/10.22034/jchemlett.2023.363900.1088

[29] E. Vessally, R. Rzayev, B. Azizi, P. Sharma and A. Kumar, Enhanced performance of a promising Au/TMDC heterostructure composed of MoTe2 nanosheets decorated with Au5 clusters: A DFT study. *Comput. Theor. Chem.*, 1242 (2024) 114933. https://doi.org/10.1016/j.comptc.2024.114933

[30] F. Behmagham, S. Arshadi, E. Vessally, T. G. Naghiyev, R. Rzayev, D. Sur et al., Adsorption of sarin on zigzag boron-nitride nanotubes (BNNTs) via DFT. *Comput. Theor. Chem.*, 1243 (2025) 114976. https://doi.org/10.1016/j.comptc.2024.114976

[31] S. Ghorbaninezhad and R. Ghiasi, Computational Investigation of β-hydrogen Elimination in the (C2X5)2B(C2H5); X=H, F, Cl, Br Molecules. *Chem. Methodol.*, 4 (2020) 80-91. https://doi.org/10.33945/SAMI/CHEMM.2020.1.7

[32] E. S. Ansari, R. Ghiasi and A. Forghaniha, Thermodynamic and kinetic studies of the retro-Diels-Alder reaction of 1,4-cyclohexadiene, 4H-pyran 4H-thiopyran, 1,4-dioxine, and 1,4-dithiine: a theoretical investigation. *Struct. Chem.*, 30 (2019) 877-885. https://doi.org/10.1007/s11224-018-1241-y

[33] M. Ahraminejad, R. Ghiasi, B. Mohtat and R. Ahmadi, substituent effect in [2+4] diels–alder cycloaddition reactions of anthracene with C2X2 (x = H, F, Cl, Me): a computational investigation. *J. Struct. Chem.*, 62 (2021) 1551-1562. https://doi.org/10.1134/S0022476621100097

[34] B. Mohammadi and M. R. Jalali Sarvestani, A Comparative Computational Investigation on Amantadine Adsorption on the Surfaces of Pristine, C-, Si-, and Ga-doped Aluminum Nitride Nanosheets. *J. Chem. Lett.*, 4 (2023) 66-70. https://doi.org/10.22034/jchemlett.2023.388369.1107

[35] S. Mirsadeghi, A. Soroush, H. Zandavar, R. Behjatmanesh-Ardakani and S. M. Pourmortazavi, Experimental and DFT-validated development of MgV2O4/Cu2V2O7 Z-scheme nanocomposites for visible-light photocatalytic degradation of imatinib. *J. Phys. Chem. Solids*, 208 (2026) 113122. https://doi.org/10.1016/j.jpcs.2025.113122

[36] R. Behjatmanesh-Ardakani and A. Moradzadeh, Band Gap Engineering of TiO2 Anatase through Cobalt and Nitrogen Co-doping: A Periodic Hybrid-DFT Study. *Phys. Chem. Res.*, 12 (2024) 763-770. https://doi.org/10.22036/pcr.2024.424372.2447

[37] R. Behjatmanesh-Ardakani, A. Moradzadeh and T. T. Magkoev, Electronic band gap calculation of N, Co, and (N, Co) single- and dual-doped rutile phase: a hybrid periodic DFT study. *Iran. J. Catal.*, 14 (2024). https://doi.org/10.57647/j.ijc.2024.1402.14

[38] R. Behjatmanesh-Ardakani, Theoretical Insights into Band Gap Tuning Through Cu Doping and Ga Vacancy in GaSe Monolayer: A First-Principles Perspective. *J. Electron. Mater.*, 53 (2024) 2398-2409. https://doi.org/10.1007/s11664-024-10977-2

[39] R. Behjatmanesh-Ardakani and A. Moradzadeh, Dual surface doping of Co+N in the anatase TiO2(100) for water splitting process. *Chem. Rev. Lett.*, 7 (2024) 17-19. https://doi.org/10.22034/crl.2024.435210.1278

[40] S. M. Ghoreishian, K. S. Ranjith, M. Ghasemi, B. Park, S.-K. Hwang, N. Irannejad et al., Engineering the photocatalytic performance of B-C3N4@Bi2S3 hybrid heterostructures for full-spectrum-driven Cr(VI) reduction and in-situ H2O2 generation: Experimental and DFT studies. *Chem. Eng. J.*, 452 (2023) 139435. https://doi.org/10.1016/j.cej.2022.139435

[41] M. A. rafiee and M. Javaheri, Theoretical Study of Benzoquinone Derivatives as Organic Cathode Materials in Lithium-Ion Batteries. *J. Chem. Lett.*, 6 (2025) 166-174. https://doi.org/10.22034/jchemlett.2025.516569.1295

[42] E. Vessally, M. R. Ilghami and M. Abbasian, Investigation the Capability of Doped Graphene Nanostructure in Magnesium and Barium Batteries with Quantum Calculations. *Chem. Res. Tech.*, 1 (2024). https://doi.org/10.2234/chemrestec.2024.436837.1007

[43] A. John, A. Uzairu, G. A. Shallangwa and S. Uba, Theoretical Investigation and Design of Novel Cephalosporin Based Inhibitors of a DD-carboxypeptidase Enzyme of Salmonella typhimurium. *J. Chem. Lett.*, 4 (2023) 52-58. https://doi.org/10.22034/jchemlett.2022.361586.1085

[44] M. R. Jalali Sarvestani and S. Majedi, A DFT study on the interaction of alprazolam with fullerene (C20). *J. Chem. Lett.*, 1 (2020) 32-38. https://doi.org/10.22034/jchemlett.2020.108111

[45] S. Abrahi Vahed, Fullerene (C20) as a Sensor for Detection of Midazolam: Theoretical Insights. *J. Med. Med. Chem.*, 1 (2025) 106-110. https://doi.org/10.22034/jmedchem.2025.547513.1019

[46] F. Najafi, S. Sattari alamdar and E. h. Vaziri, Fullerene (C20) as a Sensor for the Detection of Nordazepam: DFT Simulations. *J. Med. Med. Chem.*, 1 (2025) 18-23. https://doi.org/10.22034/jmedchem.2025.526412.1004

[47] N. Mirderikvand and M. Mahboubi-Rabbani, A DFT Study on Citalopram Adsorption on the Surface of B12N12. *J. Chem. Tech.*, 1 (2025) 90-95. https://doi.org/10.22034/jchemtech.2025.538393.1015

[48] N. Mirderikvand and M. Bayanati, Chlorpromazine Adsorption on the Surface of Fullerene (C20): DFT Insights. *J. Chem. Tech.* (2025). https://doi.org/10.22034/jchemtech.2025.552799.1027

[49] M. R. Poor Heravi, B. Azizi, E. Abdulkareem Mahmood, A. G. Ebadi, M. J. Ansari and S. Soleimani-Amiri, Molecular simulation of the paracetamol drug interaction with Pt-decorated BC3 graphene-like nanosheet. *Mol. Simul.*, 48 (2022) 517-525. https://doi.org/10.1080/08927022.2022.2030861

[50] S. Esfahani, J. Akbari, S. Soleimani-Amiri, M. Mirzaei and A. Ghasemi Gol, Assessing the drug delivery of ibuprofen by the assistance of metal-doped graphenes: Insights from density functional theory. *Diamond Relat. Mater.*, 135 (2023) 109893. https://doi.org/10.1016/j.diamond.2023.109893

[51] S. Esfahani, J. Akbari and S. Soleimani-Amiri, Adsorption of Ibuprofen by an Iron-doped Silicon Carbide Graphene monolayer: DFT exploration of drug delivery insights. *Int. J. Nano Dimension*, 15 (2024) 63-71. https://doi.org/10.22034/ijnd.2023.1995303.2253

[52] A. S. Hessen, N. M. Ahmed Alsultany, H. Bahir, A. H. Adthab, S. Soleimani-Amiri and S. Ahmadi et al., Adsorption of sulfur mustard on the transition metals (TM = Ti2+, Cr2+, Fe2+, Co2+, Ni2+, Cu2+, Zn2+) porphyrins induced in carbon nanocone (TM-PCNC): Insight from DFT calculation. *J. Mol. Graph. Model.*, 135 (2025) 108928. https://doi.org/10.1016/j.jmgm.2024.108928

[53] A. Karbakhshzadeh, S. Majedi and V. Abbasi, Computational investigation on interaction between graphene nanostructure BC3 and Rimantadine drug: Possible sensing study of BC3 and its doped derivatives on Rimantadine. *J. Chem. Lett.*, 3 (2022) 108-113. https://doi.org/10.22034/jchemlett.2022.352857.1079

[54] M. Mosavi, Adsorption behavior of mephentermine on the pristine and Si, Al, Ga- doped boron nitride nanosheets: DFT studies. *J. Chem. Lett.*, 1 (2020) 164-171. https://doi.org/10.22034/jchemlett.2022.330189.1057

[55] R. Ahmadi, Furazolidone Adsorption on the Surface of B12N12: DFT Simulations. *J. Med. Med. Chem.*, 1 (2025) 100-105. https://doi.org/10.22034/jmedchem.2025.547065.1018

[56] E. Vessally, B. Azizi, Q. Husam Aziz, K. R. Al-Shami, H. Tariq and F. Behmagham et al., DFT, TD-DFT, QTAIM and NBO investigations of the interaction between sulfur mustard and metal porphyrins induced in carbon nanocone (M-PCNC, M = Fe2+ and Mg2+). *J. Sulfur Chem.*, 46 (2025) 291-311. https://doi.org/10.1080/17415993.2025.2457347

[57] B. Azizi, R. Rzayev and E. Vessally, Enhanced chemical activity and gas sensing performance of silicene nanosheets by noble metal (Au, Ag) decoration: A DFT study. *Comput. Theor. Chem.*, 1242 (2024) 114949. https://doi.org/10.1016/j.comptc.2024.114949

[58] B. Delley, From molecules to solids with the DMol3 approach. *J. Chem. Phys.*, 113 (2000) 7756-7764. https://doi.org/10.1063/1.1316015

[59] M. J. Frisch, G. W. Trucks, H. B. Schlegel, G. E. Scuseria, M. A. Robb and J. R. Cheeseman et al., Gaussian 16 Rev. A.01, Gaussian, Inc., Wallingford CT (2016).

[60] T. Lu and F. Chen, Multiwfn: A multifunctional wavefunction analyzer. *J. Comput. Chem.*, 33 (2012) 580-592. https://doi.org/10.1002/jcc.22885

[61] R. Dennington, T. A. Keith and J. M. Millam, GaussView, Version 5.0, Semichem Inc., Shawnee Mission, KS (2016).

[62] J. P. Perdew, K. Burke and M. Ernzerhof, Generalized Gradient Approximation Made Simple. *Phys. Rev. Lett.*, 77 (1996) 3865-3868. https://doi.org/10.1103/PhysRevLett.77.3865

[63] S. Grimme, Semiempirical GGA-type density functional constructed with a long-range dispersion correction. *J. Comput. Chem.*, 27 (2006) 1787-1799. https://doi.org/10.1002/jcc.20495

[64] Z.-Y. Qiu and J.-S. Dang, Mechanistic studies on defective hBN-supported metal-nonmetal synergistic catalysis for urea electrosynthesis. *Appl. Surf. Sci.*, 679 (2025) 161230. https://doi.org/10.1016/j.apsusc.2024.161230

[65] R. Behjatmanesh-Ardakani and A. Heydari, Molecular and dissociative adsorption of tetrachlorodibenzodioxin on M-doped graphenes (M = B, Al, N, P): pure DFT and DFT + VdW calculations. *J. Mol. Model.*, 26 (2020) 164. https://doi.org/10.1007/s00894-020-04387-4

[66] R. Behjatmanesh-Ardakani, E. M. Bahalkeh and V. Moeini, A mechanistic periodic DFT study of CH, CO, and OH dissociations in methanol: M-doped carbon nanotubes (M=Pt, B, Al, N, P) versus Pt(100), Pt(110) and Pt(111) surfaces. *Mol. Catal.*, 512 (2021) 111781. https://doi.org/10.1016/j.mcat.2021.111781

[67] R. Behjatmanesh-Ardakani, Periodic hybrid-DFT study on the N-doped TiO2 (001) nanotubes as solar water splitting catalysts: A comparison with the rutile and anatase bulk phases. *Int. J. Hydrogen Energy*, 48 (2023) 35584-35598. https://doi.org/10.1016/j.ijhydene.2023.05.352

[68] A. D. Becke, Density-functional thermochemistry. III. The role of exact exchange. *J. Chem. Phys.*, 98 (1993) 5648-5652. https://doi.org/10.1063/1.464913

[69] C. Lee, W. Yang and R. G. Parr, Development of the Colle-Salvetti correlation-energy formula into a functional of the electron density. *Phys. Rev. B*, 37 (1988) 785. https://doi.org/10.1103/PhysRevB.37.785

[70] P. J. Stephens, F. J. Devlin, C. F. Chabalowski and M. J. Frisch, Ab Initio Calculation of Vibrational Absorption and Circular Dichroism Spectra Using Density Functional Force Fields. *J. Phys. Chem.*, 98 (1994) 11623-11627. https://doi.org/10.1021/j100096a001

[71] F. Weigend and R. Ahlrichs, Balanced basis sets of split valence, triple zeta valence and quadruple zeta valence quality for H to Rn: Design and assessment of accuracy. *Phys. Chem. Chem. Phys.*, 7 (2005) 3297-3305. https://doi.org/10.1039/B508541A

[72] A. S. Faihan, T. A. Yousef, I. F. Alshdoukhi, M. Ashfaq, A. S. Al-Janabi and R. Behjatmanesh-Ardakani et al., Synthesis, characterization and biological activity of Pt(II) acesulfame with triphenylphosphine or bipyridine. Crystal structure, Hirshfield and DFT studies of [Pt(ACS)Cl(PPh3)]. *J. Mol. Struct.*, 1341 (2025) 142637. https://doi.org/10.1016/j.molstruc.2025.142637

[73] A. S. Faihan, N. M. Aziz, M. Ashfaq, R. Behjatmanesh-Ardakani, A. S. Al-Janabi and M. N. Tahir et al., Expected coordination and unexpected transformation of the bis(diphenylphosphino)methane in the platinum(II) complex. *J. Indian Chem. Soc.*, 102 (2025) 101969. https://doi.org/10.1016/j.jics.2025.101969

[74] K. A. Jasim, N. M. Aziz, M. Ashfaq, R. Behjatmanesh-Ardakani, A. S. Faihan and M. N. Tahir et al., Docking, DFT, and structural study of N-((1,5-dimethyl-3-oxo-2-phenyl-2,3-dihydro-1H-pyrazol-4-yl)carbamothioyl)benzamide. *Struct. Chem.*, 35 (2024) 1411-1425. https://doi.org/10.1007/s11224-024-02278-5

[75] E. Sheikh Ansari, R. Ghiasi and A. Forghaniha, Computational Investigation into the Solvent Effect on the Diels-Alder Reaction of Isobenzofuran and Ethylene. *Chem. Methodol.*, 4 (2020) 220-233. https://doi.org/10.33945/SAMI/CHEMM/2020.3.1

[76] S. Kamrava, R. Ghiasi and A. Marjani, The conductor-like polarizable continuum model study of indenyl effect on the ligand substitution reaction in the (η5-C9H7)Co(CO)2 complex. *Int. J. Chem. Kinet.*, 53 (2021) 901-912. https://doi.org/10.1002/kin.21491

[77] R. Behjatmanesh-Ardakani and H. Imanov, DFT study on the mechanism of benzimidazole synthesis from phenylenediamine and formic acid: activation energies and transition states' locations. *Chem. Rev. Lett.* (2025). http://doi.org/10.22034/crl.2025.537649.1665

[78] P. A. Redhead, Thermal desorption of gases. *Vacuum*, 12 (1962) 203-211. https://doi.org/10.1016/0042-207X(62)90978-8